Astronomy & Astrophysics manuscript no. paper
February 27, 2015

Efficient numerical implementation of non-ideal equations of state for astrophysical fluid simulations

B. Vaidya[1], A. Mignone[1], G. Bodo[2], and S. Massaglia[1]

[1] Dipartimento di Fisica, Univesità di Torino, via Pietro Giuria 1, I-10125 Torino, Italy
[2] INAF, Osservatorio Astronomico di Torino, Strada Osservatorio 20, I-10025 Pino Torinese, Italy

Received date / Accepted date

ABSTRACT

Context. An Equation of State (*EoS*) is a relation between thermodynamic state variables and it is essential for closing the set of equations describing a fluid system. Although an ideal EoS with a constant *adiabatic index* Γ is the preferred choice due to its simplistic implementation, many astrophysical fluid simulations may benefit from a more sophisticated *EoS* (temperature-dependent Γ) which can account for diverse chemical processes.

Aims. In the present work we first review the basic thermodynamical principles of a gas mixture in terms of its thermal and caloric EoS by including fundamental processes such as atomic translation and ionization as well as molecular vibrations and rotations. The formulation is revisited in the context of plasmas that are either in equilibrium conditions (local thermodynamic- or collisional excitation- equilibria) or described by non-equilibrium chemistry coupled to optically thin radiative cooling.
We then describe a numerical implementation to model thermally ideal gases obeying a caloric EoS with non-constant adiabatic index in Godunov-type numerical schemes.

Methods. We address the problems of conversion between internal energy and pressure, sound speed computation (needed by the Riemann solver) and thermodynamic consistency. Two alternative numerical approaches are presented. The first one, best suited for EoS in analytical form, employs root-finder methods while the second one leans on lookup table and spline interpolation and can be also used for EoS in tabulated form.

Results. The two approaches are compared in terms of speed, accuracy. Our results indicate that the inclusion of a general EoS is better handled by using tables (whenever possible) and it involves a code slow down of a factor of ... Using tables gives a speed up of a factor... for some problems and it is more general for EoS that do not have analytical form.

Key words. Equation of state – Methods: numerical – Atomic processes – Molecular processes – Shock waves

1. Introduction

The equation of state is a fundamental characteristic of a substance which makes possible the application of the general principles of thermodynamics to physical objects. For a complete mathematical description of dynamics in fluids, the conservation laws of mass, momentum and energy. must be supplemented with an EoS. Numerical simulations of astrophysical systems such as inter-stellar medium, planetary atmospheres, stellar evolution, jets and outflows, require inter-play of various thermal, radiative and chemical processes. For such complex systems, using a simple ideal (or an isothermal) EoS would be considered as a serious limitation. A consistent description for such systems demands the use of a *general EoS* that can account thermal and chemical processes.

Thermodynamic state of the gas plays a pivotal role in governing the fragmentation of self-gravitating and turbulent molecular clouds (e.g., Spaans & Silk 2000; Li et al. 2003; Jappsen et al. 2005). The balance of heating and cooling in molecular clouds is approximated using a poly-tropic EoS, $p \propto \rho^{\Gamma}$. Multiple smoothed particle hydrodynamical simulations with different adiabatic indices, $0.2 < \Gamma < 1.4$ (Spaans & Silk 2000) was used to show that the degree of fragmentation decreases with increasing value of Γ (Li et al. 2003). Jappsen et al. (2005) showed that the thermal properties of the gas determines the stellar mass function (IMF) using a piecewise poly-tropic EoS. Such empirical forms of EoS in general depend on chemical abundances and complex atomic and molecular physics.

Numerical simulations studying thermo-chemical evolution of early structure formation used an *effective* adiabatic index, $\Gamma_{\rm eff}$, to relate internal energy with thermal pressure (e.g. Yoshida et al. 2006; Glover & Abel 2008). The value of $\Gamma_{\rm eff}$ is estimated from number fractions of chemical species treating the chemical composition as an ideal mixture. In the context of disk instability leading to formation of gas giant planets, Boley et al. (2007) pointed out the importance of incorporating isotopic forms of molecular hydrogen, H_2, as well the molecular physics (rotation and vibration) under thermodynamic equilibrium in the estimate of internal energy. A more complex EoS taking into account ionization from atomic hydrogen and helium along with molecular dissociations is used to study the envelopes of young planetary cores (D'Angelo & Bodenheimer 2013).

The goal of this paper is to outline a consistent numerical framework for the implementation of a more general equation of state in the context of the magnetohydrodynamics (MHD) equations. Our formulation accounts for different physical processes such as atomic ionization and recombination, molecular dissociation, etc... and it is suitable under equilibrium conditions (local thermodynamic or collisional ionization equilibria) as well as for non-equilibrium optically thin radiative cooling (Teşileanu et al. 2008). The numerical method is implemented as part of the PLUTO code (Mignone et al. 2007) and it is built while ensur-

ing thermodynamical consistency, accuracy and computational efficiency.

Our starting point are the ideal MHD equations written in conservation form:

$$\frac{\partial \rho}{\partial t} + \nabla \cdot (\rho \mathbf{v}) = 0 \tag{1}$$

$$\frac{\partial (\rho \mathbf{v})}{\partial t} + \nabla \cdot \left(\rho \mathbf{v}\mathbf{v}^T - \mathbf{B}\mathbf{B}^T \right) + \nabla p_t = 0 \tag{2}$$

$$\frac{\partial \mathbf{B}}{\partial t} - \nabla \times (\mathbf{v} \times \mathbf{B}) = \mathbf{0} \tag{3}$$

$$\frac{\partial E}{\partial t} + \nabla \cdot \left[(E + p_t)\, \mathbf{v} - (\mathbf{v} \cdot \mathbf{B})\, \mathbf{B} \right] = \Lambda \tag{4}$$

$$\frac{\partial (\rho X_k)}{\partial t} + \nabla \cdot (\rho X_k \mathbf{v}) = S_k \tag{5}$$

where ρ is the mass density, $\mathbf{v}$ is the fluid velocity, $\mathbf{B}$ is the magnetic field, $p_t = p + \mathbf{B}^2/2$ is the total pressure accounting for thermal (p) and magnetic ($\mathbf{B}^2/2$) contributions. The total energy density E is given by

$$E = \rho e + \frac{1}{2}\rho \mathbf{v}^2 + \frac{1}{2}\mathbf{B}^2 . \tag{6}$$

An additional EoS relating the internal energy density ρe with p and ρ must be specified. This issue is addressed in §2. Dissipative effects have been neglected for the sake of exposition although they can be easily incorporated in this framework.

The paper is organized as follows, in §2 the basic principles and formulations of general *EoS* used for the present work are described. The numerical framework is discussed in §3. The results obtained from various test problems are outlined in §4 and the concluding remarks are summarized in §5 .

2. Equation of State

2.1. Thermodynamical Principles

A physical system is characterized by *extensive* and *intensive* properties. An intensive variable is the one that does not depend on the bulk properties (volume) of the system, and an extensive variable is one that does. From the thermodynamic point of view, equilibrium states of physical systems, macroscopically, are completely defined by the relation between the differentials of extensive properties like the internal energy U and the volume V along with the definition of the entropy $S(U, V)$. This is known as the first law of thermodynamics and is given by

$$dU = TdS - pdV. \tag{7}$$

Here, the temperature T and pressure p are referred to as intensive properties. An *EoS* of such a system is defined as a relation among intensive and extensive properties. It can be broadly classified into two types. The *thermal EoS* is defined as the expression of pressure in terms of volume and temperature $p = p(V, \mathrm{T})$. Whereas, the *caloric EoS* specifies the dependence of the internal energy of the system U on volume V and temperature T.

In general, these relations are derived from empirical results and are used to estimate various thermodynamic properties of a system. Theoretically, statistical principles can be applied to describe such a system on basis of its microscopic processes using partition function, $\mathcal{Z}$. For example, the macroscopic thermodynamic quantities can be obtained from the following standard relations,

$$\begin{aligned} p &= k_B T \left(\tfrac{\partial ln \mathcal{Z}}{\partial V} \right)_T \\ U &= k_B T^2 \left(\tfrac{\partial ln \mathcal{Z}}{\partial T} \right)_V , \end{aligned} \tag{8}$$

where, k_B is the Boltzmann constant. The above equation essentially provides two forms of *EoS* in terms of partition function.

In the present work, our focus will be mainly for *thermally ideal gas*. These gases have their thermal EoS same as that of an ideal gas. However, their caloric EoS can have non-linear dependence on temperature based on various chemical processes taken into consideration (see §2.2). Though, the analysis presented here is limited to thermally ideal gas, the numerical implementation described in this work can also be extended to study real gases obeying thermal EoS given by van der Waals.

2.2. Thermally Ideal Gas

Consider a case of classical monoatomic ideal gas, where, the partition function $\mathcal{Z}$ is given by,

$$\mathcal{Z} = \frac{1}{N!} \left[\left(\frac{m k_B T}{2\pi\hbar^2} \right)^{3/2} V \right]^N , \tag{9}$$

where, m is the mass of the particle, $\hbar$ the Planck constant and N the total number of non-interacting particles. On substituting Eq.9 in Eq.8, we obtain the standard forms of *EoS* for a classical ideal gas,

$$\begin{aligned} pV &= N k_B T \\ U &= \tfrac{3}{2} N k_B T = C_V T, \end{aligned} \tag{10}$$

where, the specific heat capacity at constant volume, C_V, is independent of temperature. On extending this analysis further to diatomic ideal gas, the partition function $\mathcal{Z}$ contains contribution from rotational and vibrational degrees of freedom, in addition to the translational motion. In such a case, the internal energy U derived from Eq.8 is given by,

$$U = \frac{3}{2} N k_B T + N k_B T + \Phi_{\mathrm{vib}}(T) \tag{11}$$

where the additional contribution of $N k_B T$ comes from rotational degree of freedom and $\Phi_{\mathrm{vib}}(T)$ denotes term due to vibrational motion which has a non-linear dependence on temperature. On considering the diatomic molecule with two degrees of freedom (i.e, translational and rotational) and neglecting the non-linear dependence due to vibration, one obtains a single relation for both monoatomic and diatomic gas by adopting a constant Γ,

$$pV = (\Gamma - 1)U, \tag{12}$$

where the value of $\Gamma = 5/3$ for monoatomic gas and 7/5 for diatomic gas (see Eqns. 10 and 11). Note that in deriving Eq. 12, it is also assumed that the diatomic gas is thermally ideal and follows the same thermal EoS (i.e., $\mathrm{pV} = \mathrm{Nk_B T}$) as that of a classical monoatomic gas. The constant Γ that depends on degree of freedom in the gas is essentially the ratio of isobaric to isochoric specific heats and also determines the sound speed, c_s, in the gas,

$$c_s = \sqrt{\left(\frac{\Gamma p}{\rho} \right)}, \tag{13}$$

where, the density of the gas $\rho = (\mathrm{N}\mu\, \mathrm{m}/V)$, μ being the mean molecular weight.

2.3. Partially Ionized Gas

Astrophysical fluids and processes are more complex than a simple system of ideal gas described above. For example, the Inter-Stellar Medium (ISM) that largely comprises of hydrogen and helium is affected by many physical and chemical processes viz., collisional ionization, dissociation, shocks, radiation etc. In such a scenario, an heuristic approach of treating it as an monoatomic ideal gas with with constant $\Gamma = 5/3$ will only be approximate and fail to account for the feedback of the above processes on thermal properties of the gas and thereby also on its inter-linked dynamics.

Here we consider a simplest case of partially ionized gas of pure hydrogen (in atomic form). The thermodynamics of such a system is different than that of a completely ionized (or completely neutral) gas. The differences occur due to non-constant number of free particles and the additional energy required during the process of ionization. The internal energy U is therefore given by (Clayton 1984),

$$U = \frac{3}{2} N k_B T + \chi_H N_{HII}. \tag{14}$$

In addition to the standard form of translational energy, contribution from ionization potential, χ_H, is included in Eq. 14. Here, N_{HII} is the number of ionized hydrogens and the total number of free particles, $N = N_H + 2N_{HII}$, is the sum of number of neutral hydrogens and two times that of N_{HII} due to charge neutrality.

In regions of dense stellar interior, one can approximate conditions to be in local thermodynamic equilibrium. For such a system, the different fractions of pure hydrogen gas has a non-linear dependence on temperature and density of the gas using the Saha equation. As a result, even the internal energy, specific heats and the adiabatic index Γ will depend on the ionization fraction. For example, the adiabatic index, Γ will smoothly change from its monoatomic value of 5/3 to 1.13 for a hydrogen gas with an ionization fraction of 50% at $T = 10^4$ K (Clayton 1984). Such a significant change in Γ is due to the fact that some part of the energy input goes into ionization rather than increasing the temperature of the gas. Therefore, using a constant value of Γ for such dense stellar interiors will considerably overestimate the temperature of gas.

2.4. Hydrogen Gas Thermodynamics at Equilibrium

Numerical simulations of various astrophysical problems up-till now have limited the use of *EoS* either in the adiabatic or the isothermal (c_s = constant) limit. Though, in some cases, these assumptions may be valid but in general they may give large deviations from the real behavior. However, in recent years, a large emphasis is given on applying an *EoS* that could take into account some of the complex astrophysical processes. Specifically, studies related to planet formation in accretion disks have started to incorporate *EoS* that can account for contribution from dissociation of molecular hydrogen, ionization of atomic hydrogen and helium and radiation (e.g., Boley et al. 2007; D'Angelo & Bodenheimer 2013) under an assumption of local thermodynamic equilibrium (LTE).

In LTE, processes like ionization and dissociation for hydrogen are given by,

$$\begin{aligned} H + e^- &\rightleftharpoons H^+ + 2e^- \\ H + H &\rightleftharpoons H_2, \end{aligned} \tag{15}$$

respectively. Following D'Angelo & Bodenheimer (2013), we define the degree of dissociation y and degree of ionization x as,

$$\begin{aligned} y &= \frac{\rho_{HI}}{\rho_{HI}+\rho_{H2}} \\ x &= \frac{\rho_{HII}}{\rho_{HI}+\rho_{HII}}, \end{aligned} \tag{16}$$

where, ρ_{HI} is the density of atomic hydrogen, ρ_{H2} the density of molecular hydrogen and ρ_{HII} the density of ionized hydrogen. In the limit of LTE, one assumes that level populations due to ionization (and dissociation) process follow Boltzmann excitation formula and the ejected free electrons thermalize to attain Maxwell-Boltzmann velocity distribution corresponding to single gas temperature. This is generally true in regions of high density like that of the solar interior. In such cases, the degree of ionization using Saha equations is given as follows,

$$\frac{x^2}{1-x} = \frac{m_H}{X\rho}\left(\frac{m_e k_B T}{2\pi\hbar^2}\right)^{3/2} e^{-13.60eV/(k_B T)}. \tag{17}$$

and also degree of dissociation, y can be obtained in a similar manner (Black & Bodenheimer 1975),

$$\frac{y^2}{1-y} = \frac{m_H}{2X\rho}\left(\frac{m_H k_B T}{4\pi\hbar^2}\right)^{3/2} e^{-4.48eV/(k_B T)}, \tag{18}$$

The gas is essentially a mixture of hydrogen in all forms (atoms, ions & molecules) with a mass fraction of X, Helium with a mass fraction of Y and negligible fraction of metals. For such a composition, the total density of gas is defined as $\rho = (N/V)\mu m_H = n\mu m_H$, where n is the number density and the mean molecular weight, μ, can be expressed as (e.g., Black & Bodenheimer 1975),

$$\frac{\mu}{4} = \left[2X(1 + y + 2xy) + Y\right]^{-1}. \tag{19}$$

Such a gas mixture is further assumed to be ideal and thus the pressure p of the gas can relate to the temperature T as, $p = \rho k_B T/(\mu m_H)$.

The most crucial part is to express a caloric *EoS* that can account for contributions from various degrees of freedom and processes like ionization and dissociation. Thus, the gas internal energy density, $(\rho e)_{gas} = (U/V)$, of the mixture is given by,

$$(\rho e)_{gas} = (\epsilon_{H2} + \epsilon_{HI} + \epsilon_{HII} + \epsilon_{H+H} + \epsilon_{He})\frac{k_B T \rho}{m_H}, \tag{20}$$

where, each term in the parenthesis is dimensionless and can be obtained from an appropriate partition function $\mathcal{Z}$ and using Eq.10. Tab. 1 summarizes the different contribution to the gas internal energy. In case of molecular hydrogen, ϵ_{H2}, terms that correspond to vibrational and rotational degree of freedom are also considered. These terms are evaluated using the partition function of vibration, ζ_v, and rotation ζ_r, that have explicit and a non-linear dependence on temperature. Additionally, the rotational partition function also takes into account the para/ortho H_2 spin states (Boley et al. 2007). Thus, the total gas internal energy density has a non-linear dependence on the temperature T and density through x and y (see Eqns. 17 & 18). In such a case, the sound speed in the gas adopts a more general definition,

$$c_s = \sqrt{\left(\frac{\Gamma_1 p}{\rho}\right)}, \tag{21}$$

Table 1. Summary of different contributions to the gas internal energy $(\rho e)_{gas}$, which is expressed using Eq.20. (see Black & Bodenheimer (1975); D'Angelo & Bodenheimer (2013))

Term	Expression	Description
ϵ_{HI}	1.5X (1 + x) y	Translational energy for hydrogen
ϵ_{He}	0.375Y	Translational energy for helium
ϵ_{H+H}	4.48 eV $X\,y/(2k_BT)$	Dissociation energy for molecular hydrogen
ϵ_{HII}	13.6 eV $X\,x\,y/(k_BT)$	Ionization energy for atomic hydrogen
ϵ_{H2}	$\frac{X(1-y)}{2}\left[1.5+\frac{T}{\zeta_v}\frac{d\zeta_v}{dT}+\frac{T}{\zeta_r}\frac{d\zeta_r}{dT}\right]$	Internal energy for molecular hydrogen

where, Γ_1 is the first adiabatic exponent. For an ideal gas with a constant C_V, $\Gamma_1 = \gamma$, however, in the general case it is given by,

$$\Gamma_1 = \frac{1}{C_V(T)}\left(\frac{p}{\rho T}\right)\chi_T^2 + \chi_\rho, \tag{22}$$

where, C_V is obtained by taking the derivative of specific gas internal energy, e_{gas}, with temperature and χ_T and χ_P are referred to as temperature and density exponents (see D'Angelo & Bodenheimer (2013)).

The left and middle panels of Fig.1 shows the variation of $\mu(\rho, T)$ (Eq. 19) and gas internal energy in ergs with temperature, T, for four values of density in g cm^{-3} respectively. The values of μ are bounded between an upper bound ∼2.3, corresponding to a fully molecular medium at low temperatures, to a small value of ∼ 0.6 at high temperatures representing fully ionized medium. The transition between these bounds is smooth at high densities $\rho = 10^{-4}$ g cm^{-3}, while, its steep with a formation of a plateau at T ∼ 10^3 *K* for low density values (black curve). The first transition occurs in a temperature range where the molecules begin to dissociate to form atomic hydrogen. Also, the temperature where the atomic hydrogen ionize show a distinct fall in values of μ. These two temperature ranges are clearly seen in the curve of internal energy with temperature T as a steep bumps. Physically, they indicate that the energy at these temperatures is going to dissociate or ionize the gas, instead of heating the gas and so the temperature remains approximately constant. Apart from these transition regions, the dependence of $(\rho e)_{gas}(m_H/\rho)$ is linear and increases monotonically with gas temperature. The last panel of the same figure shows the variation of first adiabatic exponent, Γ_1 with temperature. At low temperatures, the gas behaves as a monoatomic ideal gas undergoing adiabatic process with a Γ_1 = 5/3. This is also true at very high temperatures where the gas comprises of ions and electrons. As anticipated from above arguments of rise in internal energy, we see a sharp decrease in values of Γ_1 from its maximum value of 5/3 to close to unity (corresponding to an isothermal limit) for a low density (black curve), while the red curve corresponding to high density shows a single dip in value at T > 10^4 K.

Such an *EoS* that accounts for ionization and dissociation for dense accretion disks in the LTE limit is being implemented in the PLUTO code and its effects on dynamics has been studied in details using standard test problems. Further, not all astrophysical problems can be approximated to be in the LTE limit. A classical case is that of a jet, where the recombination time scales are comparable to that of dynamical time. In such a scenario, LTE assumptions become invalid and a non-equilibrium approach has to be adopted as described in the following section.

2.5. Non-Equilibrium Hydrogen Chemistry

Astrophysical flows in HII regions, supernova remnants, star forming regions are some classical examples where optically thin cooling time scales are comparable to the dynamical time. In such environments, ionization and dissociation fractions are far from equilibrium and their estimation based on Saha fractions can give large errors. Thus in such non-equilibrium regions, number density of various species are determined by solving the chemical rate equations, which have a general form as,

$$\frac{dn_i}{dt} = \sum_{j,k}\mathcal{K}_{j,k}n_jn_k - n_i\sum_j\mathcal{K}_{i,j}n_j, \tag{23}$$

where, n is the number density, $\mathcal{K}_{j,k}$ is the rate of formation of ith specie from all j and k species and $\mathcal{K}_{i,j}$is the rate of destruction of ith specie due to all j species. In dilute regions such as the solar corona, Eq. 23 can be simplified by setting $dn_i/dt = 0$, as the time scales are such that a balance is always maintained between collisional ionization and radiative recombination. This is known as *Coronal equilibrium* or *Collisional Ionization Equilibrium (CIE)*. Such an equilibrium is different from LTE in two aspects. It is only valid in dilute plasma unlike the LTE where high density environments are required and the ionization fraction are estimated using Eq.23 in steady state and not with Saha fractions.

For the present purpose, we have focused only in evolving the chemical equations involving atomic and molecular hydrogen. This prescription of molecular cooling has been added to the PLUTO code to study the chemical evolution of hydrogen species. In particular, the total hydrogen number density n_H comprises of contribution from atomic and molecular hydrogen i.e., $n_H = n_{HI} + 2.0*n_{H2} + n_{HII}$. The contribution to electrons, n_e, comes from the ionized hydrogen, n_{HII} and from small but fixed fraction of metals ($Z \sim 10^{-4}$). In addition to hydrogen, helium is present with a fixed mass fraction of 0.027. The total number of particle density, i.e, $n_{tot} = n_H + n_{He} + n_e$ is always conserved as the mass density $\rho = \mu\, n_{tot}\, m_p$ is treated as a conservative variable in the code.

The chemical evolution of molecular, atomic and ionized hydrogen is governed by equations listed in Tab. 2. The code tracks the formation and destruction of these three species based on the temperature dependent reaction rates specified and updates their respective fractions viz.,

$$X_{HI} = \frac{n_{HI}}{n_H}; X_{H2} = \frac{n_{H2}}{n_H}; X_{HII} = \frac{n_{HII}}{n_H} \tag{24}$$

Even in this slightly more complex network of reactions, one can estimate concentration of each species in equilibrium (by setting the time derivation of Eq.23 to zero). Fig. 2 shows the variation of such equilibrium concentration with temperature. The

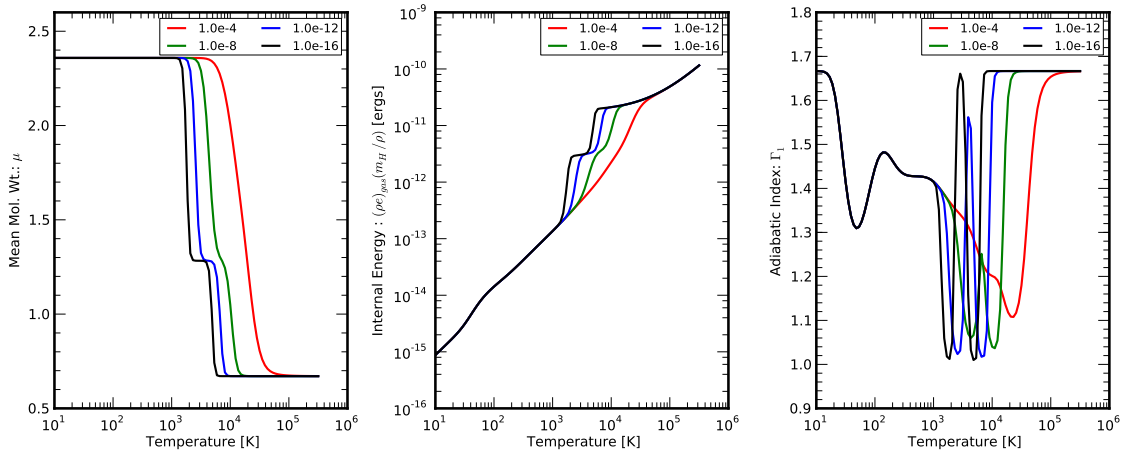

Fig. 1. Variation of Mean molecular weight μ, internal energy density of the gas $(\rho e)_{\rm gas}$ and first adiabatic index Γ_1 with temperature. The different colored curves represent four values of fixed density in g cm^{-3}, viz., 10^{-4} (*red*),10^{-8} (*green*), 10^{-12} (*blue*) and 10^{-16}(*black*). The values of $(\rho e)_{gas}$ and Γ_1 are obtained at equilibrium between ortho and para hydrogen.

Table 2. Summary of the chemistry reaction set. T is the temperature in Kelvin, $T_{\rm eV}$ is the temperature in electron-volts, $T_5 = T/1 \times 10^5$ and T_2 = T/100

No.	Reaction	Rate Coefficient (cm^{3}s^{-1})	Reference [1]
1.	$H + e^- \rightarrow H^+ + 2e^-$	$k_1 = 5.85 \times 10^{-11}\, T^{0.5}$ exp(-157,809.1/T)/(1.0 + $T_5^{0.5}$)	1
2.	$H^+ + e^- \rightarrow H + h\nu$	$k_2 = 3.5 \times 10^{-12}(T/300.0)^{-0.8}$	2
3.	$H_2 + e^- \rightarrow 2H + e^-$	$k_3 = 4.4 \times 10^{-10} T^{0.35}exp(-102,000.0/T)$	3
4.	$H_2 + H \rightarrow 3H$	$k_4 = 1.067 \times 10^{-10} T_{\rm eV}^{2.012}$(exp(4.463/T$_{\rm eV}$)$^{-1}$((1. + 0.2472T$_{\rm eV}$)$^{3.512}$)$^{-1}$	4
5.	$H_2 + H_2 \rightarrow H_2 + 2H$	$k_5 = 1.0 \times 10^{-8}$exp$(-84,100/T)$	2
6.	$H + H \xrightarrow{\rm dust} H_2$	$k_6 = 3.0 \times 10^{-17}\sqrt{T_2}(1.0 + 0.4\sqrt{T_2 + 0.15} + 0.2T_2 + 0.8T_2^2)$	5

hydrogen molecule dissociation temperature which lies around T $\sim 3 \times 10^3$ K and ionization temperature, T $\sim 10^4$ K, is very well evident from regions of transitions between species in the curve. Such equilibrium values based on temperatures are essential to initialize fractions and are used in case of Sod tube test (see Sec.4.1).

For regions where neither CIE or LTE is applicable, a general approach has to be established. Here, in addition to the time dependent estimate of number density, proper treatment should be carried out to evolve the internal energy that should also account for losses due to optically thin cooling. Such a cooling implies that the emitted photons due to different physical processes (e.g., ionization, metal line cooling etc.) freely stream (without diffusion) away from the region where they are produced and eventually escape into the surroundings resulting into an effective decrease in total gas internal energy. Thus, in addition to the conservative evolution of total energy (Eq. 4), the code accounts for the loss in gas internal energy due to cooling,

$$\frac{d(\rho e)}{dt} = -\Lambda(n, T), \tag{25}$$

where, Λ is the radiative cooling function due to losses from various processes described below,

$$\Lambda = \Lambda_{\rm CI} + \Lambda_{\rm RR} + \Lambda_{\rm rotvib} + \Lambda_{\rm H2diss} + \Lambda_{\rm grain}, \tag{26}$$

where, $\Lambda_{\rm CI}$ and $\Lambda_{\rm RR}$ are losses due to collisional ionization and radiative recombination respectively (Teşileanu et al. 2008). The remaining terms, $\Lambda_{\rm rotvib}$, $\Lambda_{\rm H2diss}$ and $\Lambda_{\rm grain}$ are associated with molecular hydrogen and represent losses due to rotational-vibrational cooling, dissociation and gas-grain processes (Smith & Rosen 2003).

In presence of cooling, the gas internal energy, $(\rho e)_{gas}$, will be different from that defined by Eq. 20. As in this case, only contributions from due translational and internal degrees of freedom (from H, He and H_2) will be incorporated, while contributions from various processes like ionization, dissociation, ro-vibrational cooling of H_2 molecule etc., will be taken care on the right hand side of Eq.25 in the Λ term. Therefore, Eq.20 now becomes,

$$(\rho e)_{gas} = (\epsilon_{H2} + \epsilon_{HI} + \epsilon_{He})\frac{k_B T \rho}{m_H}, \tag{27}$$

where, expressions for each of the internal energy components are given in table 1. Such a division of thermodynamic terms to left and right hand side of Eq. 25 has also been applied to study the role of molecular hydrogen in primordial star formation (e.g., Palla et al. 1983; Omukai & Nishi 1998).

3. Numerical Implementation

PLUTO solves the MHD equations (1)–(5) using flux-conserving form where the basic building block is

$$\mathbf{U}^{n+1} = \mathbf{U}^n - \Delta t \mathcal{L}(\mathbf{U}) \tag{28}$$

where $\mathbf{U} = (\rho, \rho\mathbf{v}, \mathbf{B}, E, \rho X_k)$ is our vector of conservative variables, see Mignone et al. (2007), Teşileanu et al. (2008) and

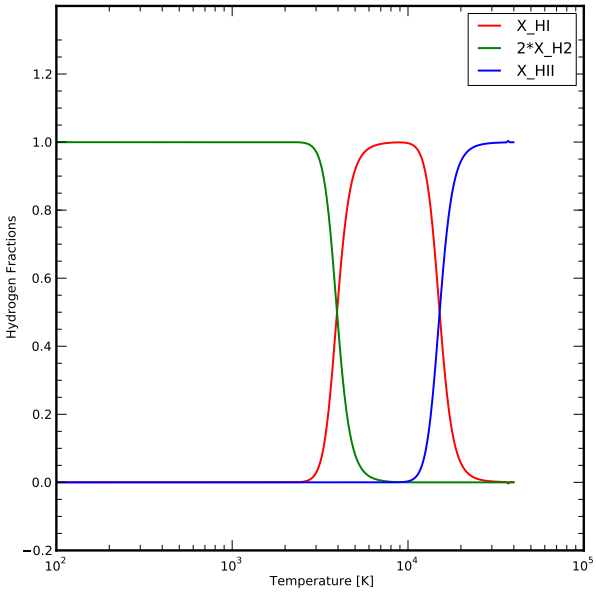

Fig. 2. Variation of different hydrogen fractions (X_HI : Atomic *red*, X_H2 : Molecular *green* and X_HII : Ionized *blue*) obtained at *equilibrium* with different temperatures. Note that the total sum of fractions, i.e, X_HI + 2.0*X_H2 + X_HII is conserved.

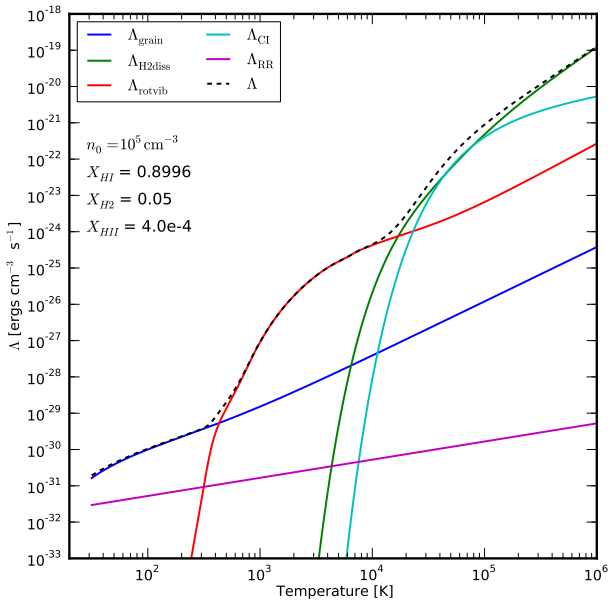

Fig. 3. The figure shows different components of radiative cooling functions with various colored lines. The values are obtained for and initial number density, $n_0 = 10^5$ cm^{-3} and fractions mentioned in the figure. The sum of all the components is drawn with a *black dashed* line to obtain the value of Λ in ergs cm^{-3} s^{-1} following Eq. 26

Mignone et al. (2012) for details. The right hand side operator $\mathcal{L}(\mathbf{U})$ carries the contributions of flux differences and source terms and it is more conveniently computed in terms of primitive variables customarily defined as $\mathbf{V} = (\rho, \mathbf{v}, \mathbf{B}, p)$. The conversion between $\mathbf{U}$ and $\mathbf{V}$ requires obtaining pressure from internal energy or viceversa. While the internal energy density is readily obtained from Eq. (6), the conversion $p \to \rho e$ and its inverse $\rho e \to p$ strictly depends on the choice of the caloric equation of state.

For the constant-Γ EoS, these transformations take a small fraction of the computational time as the relation between internal energy and pressure is straoghtforward and given by

$$\rho e = \frac{p}{\Gamma - 1}\,. \tag{29}$$

Note also that the temperature does not explicitly appears in the previous definition.

The situation is different, however, for a more general EoS where a closed-form expression between pressure and internal energy cannot be written explictly but it requires the computation of the temperature T. From the considerations given in the previous sections, in fact, we can write the thermal and caloric equations of state as

$$\begin{cases} p &= \dfrac{\rho T}{k_B m_u \mu(\mathbf{X})} \\ e &= e(T, \mathbf{X}) \end{cases} \tag{30}$$

The explicit dependence on the temperature introduces two additional intermediate steps, namely:

1. During the conversion from primitive to conservative ($p \to \rho e$) one first needs to compute T from the thermal EoS (first of Eq. 30):

$$T = \frac{p}{\rho} k_B m_u \mu(\mathbf{X}) \tag{31}$$

   Under non-equilibrium conditions, $\mu = \mu(\mathbf{X})$ is a known function of the gas composition and Eq. (31) can be solved directly. Under LTE or CIE, on the other hand, $\mathbf{X} = \mathbf{X}(T, \rho)$ is a function of density and temperature and Eq. (31) becomes a nonlinear equation in the temperature variable.
2. During the inverse transformation ($\rho e \to p$), one must first solve for the temperature by inverting

$$e = e(T, \mathbf{X})\,, \tag{32}$$

   where, under equilibrium assumptions, the chemical composition if a function of density and temperature, i.e., $\mathbf{X} = \mathbf{X}(T, \rho)$.

In order to cope with the numerical inversion of Eqns. (31) and (32) we have considered and implemented two different solution strategies that we describe in the following sections.

3.1. Inversion using root-finders

The first inversion algorithm has general validity and consists of inverting the thermal (in equilibrium conditions) and caloric EoS numerically using an iterative root-finder algorithm to recover, respectively, $T = T(p, \rho)$ and $T = T(e, \mathbf{X})$. This results in increased computational cost inasmuch the internal energy is an expensive function to evaluate. Among different root-solvers not requiring the knowledge of the derivative, we have found the Brent root-finder to be a practical and efficient method.

3.2. Inversion using Tables

A second and more efficient strategy can be used when the internal energy is a function of temperature and density alone (which is typically the case under equilibrium conditions, CIE or LTE) and it consists of employing pre-computed tables of pressure and internal energy, e.g., $\{p\}_{ij} = p(T_i, \rho_j)$ and $\{\rho e\}_{ij} = \rho e(T_i, \rho_j)$ where i and j are the table indices. For convenience, the tables are constructed using equally-spaced node values in $\log T$ and $\log \rho$ so that tabulated values are computed for $\log T_i/T_0 = i\Delta \log T$ and $\log \rho_j/\rho_0 = j\Delta \log \rho$.

When T and ρ are known, pressure and internal energy can then be retrieved by using lookup table followed by two-dimensional interpolation between adjacent node values. We first locate the table indices i and j by a simple division:

$$i = \text{floor}\left(\frac{\log T/T_0}{\Delta \log T}\right), \quad j = \text{floor}\left(\frac{\log \rho/\rho_0}{\Delta \log \rho}\right) \tag{33}$$

where T and ρ are the input values at which interpolation is desired. Internal energy (and similarly pressure) is then computed as

$$\rho e(T, \rho) = \mathcal{S}_{i,j}(x_i)(1 - y_j) + \mathcal{S}_{i,j+1}(x_i) y_j \tag{34}$$

where $x_i = (T - T_i)/(T_{i+1} - T_i)$ and $y_j = (\rho - \rho_j)/(\rho_{j+1} - \rho_j)$ are normalized coordinates between adjacent nodes while $\mathcal{S}$ is an interpolating spline.

Conversely, when ρe and ρ are known, Eq. (34) must be inverted for T. To this end, we first locate the index j using the second of (33). We then perform a binary search on the one-dimensional arrays $\{\rho e\}_{i',j}$ and $\{\rho e\}_{i',j+1}$ with i' running from 0 to $N_x - 1$ and j given by the previous equation. If the two searches result in the same index i, then the value of ρe must fall somewhere inside i and $i + 1$. Otherwise we repeat the binary search on the intermediate array $q = \{\rho e\}_{i',j}(1 - y_j) + \{\rho e\}_{i',j+1} y_j$ for $i_{\min} \le i' \le i_{\max}$ ($i_{\min}$ and $i_{\max}$ being the minimum and maximum indices of the previous search) to nail down the correct index value i.

3.2.1. On the choice of the interpolant

For linear interpolation, we simply use

$$\mathcal{S}_{i,j} = \{\rho e\}_{i+1,j} x_i + \{\rho e\}_{i,j}(1 - x_i), \tag{35}$$

and Eq. (34) becomes a bilinear interpolant. Linear interpolation, however, may generate thermodynamically inconsistent results since the positivity of the fundamental derivative is not preserved. This generates compund waves in the solution and can also violate the convexity properties of the caloric EoS. The dramatic consequence is the generation of compund waves in the Riemann fan and therefore incorrect results even for 1D problems. This is usually the case when few points are used in the temperature grid.

In order to improved the quality of interpolation, we have also implemented a cubic spline when interpolating in the temperature grid so that

$$\mathcal{S}_{i,j}(x) = a_{i,j} x_i^3 + b_{i,j} x_i^2 + c_{i,j} x_i + d_{i,j}, \tag{36}$$

where the coefficients a, b, c and d are computed by ensuring that the cubic is strictly monotonic in the interval $[T_i, T_{i+1}]$, see Wolberg & Alfy (2002). Conversely, the inverse mapping requires computing T from ρ and ρe and this is done by solving Eq. (34) for x (that is T). The solution is straightforward for bilinear interpolation while, for a monotone cubic spline, the root is found very efficiently using the Newton-Raphson method on the unit interval. The tabulated approach has found to be faster than the general root finder method giving considerable speedups up to a factor of 4 for certain problems.

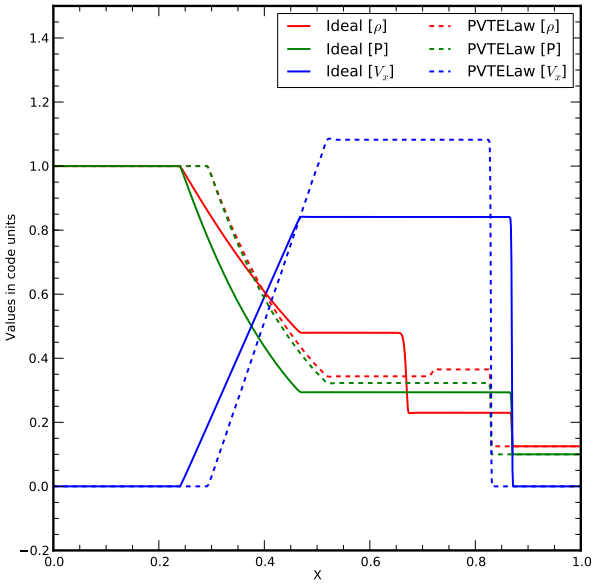

Fig. 4. The figure shows the variation of density ρ (*red*), Pressure P (*green*), and velocity v_x (*blue*) along the X-axis (in code units) for a standard Sod Tube test (without explicit cooling) at time $\tau = 0.2$. The values obtained using an ideal EoS are shown as *solid lines* while that obtained using a GammaLaw EoS are shown as *dashed lines.*

4. Results : Test Problems

The effects on inclusion of a gamma-law EoS on standard test problems with and without inclusion of explicit cooling (or chemical network) are described here.

4.1. Sod Shock Tube

The first test is that of a standard Sod Shock Tube. This is essentially an one-dimensional test using the Hydrodynamical (HD) module of the code. The numerical domain ranges from x = 0.0 to x = 1.0 having a uniform resolution, Δx = 1.0e-3. The initial setup has a static fluid (V_x = 0.0) with different temperatures across the interface at x = 0.5. The hotter region in the left has a temperature of $T_L \sim 3852\,K$ with pressure, P_L and density, ρ_L set to 1.0 in non-dimensional units. The region to the right of interface has a temperature $T_R \sim 3345\,K$ with $P_R = 0.1$ and ρ_R = 0.125. The final state at time, $\tau = 0.2$, for all relevant hydrodynamic quantities is shown figure.

The Fig. 4 compares the spatial variation of density, pressure and velocity for an Ideal EoS (*solid lines*) with that of PVTE Law *dashed lines*) without the inclusion of explicit cooling. A standard shock tube solution comprising of a rarefaction wave, contact discontinuity and a right ward propagating shock is obtained, as expected for an Ideal EoS. However with the PVTE Law, the shock tube solution is considerably different. The speed of shock propagation is much slower in case of PVTE Law, as seen from an offset in the solid and dashed curves of velocity (*blue*). Further, the offset in pressure (*green*) leftward of the interface suggests that even the propagation of rarefaction wave is slower with the PVTE Law. The most dramatic difference is seen in the evolution of density (*red*) curve at the contact discontinuity. The ideal solution of right-ward propagation contact discontinuity is absent in case of PVTE Law. Instead, a compression leading to an enhancement of density behind the shock interface is seen in the density structure with PVTE Law.

The major difference between the two EoS, is the distribution of heat into internal energy. In case of an Ideal EoS, the internal energy has contribution only from translation degree of freedom, which in 3D amount to three different directions of motions resulting in 10. While in case of PVTE Law, additional degrees of freedom due to rotation and vibration of di-atomic molecules (like H_2 at low temperatures) also contribute to the internal energy. Therefore, the energy resulting from an impact a shock in case of PVTE Law will not only populate the three 3 translational degrees of freedom, but also the vibrational and rotational levels of the molecules. Additionally, part of the energy will also be utilized for processes like dissociation and ionization that are accounted for in the formulation of PVTE Law. Therefore the amount of energy available to increase the temperature will be less in case of PVTE Law as compared to that of an Ideal EoS. Since, the fractions of ions and molecules are always assumed to be at LTE for such kind of EoS, the overall effect on application of PVTE Law EoS is that of an *equilibrium cooling*.

The above physical picture is further verified by the comparison done in the Fig. 5 between atomic (*star*) and molecular (*solid*) PVTE Law at two different temperatures (see 2.4) assuming a pure hydrogen gas (i.e., no helium or metals). The left panel shows the final state of density (*red*) and temperature (*green*) at a lower initial temperature of 120 K left of the interface and 95 K on the right. Molecular hydrogen H_2 is present at such low temperatures, thus the temperature obtained from PVTE Law that accounts for thermodynamical processes of molecules, show a different density structure from the one which just accounts for ionization. Also, the temperature behind the shock for atomic PVTE Law is around 160μ, μ being the mean molecular weight. While that for molecular PVTE Law is reduced to 140μ due to *equilibrium cooling* described above. Additionally, the density behind the shock is more condensed as expected from arguments described above for the PVTE law that accounts for presence of molecules in the system. These differences in the shock structure completely vanish when the initial temperature for the left side of interface at x = 0.5 raised to about 1.35×10^4 K At such temperatures, a complete dissociation of molecular hydrogen takes place and the molecular PVTE law essentially becomes same as that of the atomic PVTE law. This is indicated from the right panel of Fig. 5, where solutions from these different EoS overlaps with each other.

The results from the sod shock tube tests ran with explicit non-equilibrium cooling (see 2.5) are shown in Fig. 6. The two panels represent quantities for different initial conditions for temperature on either sides of the interface. The initial values of T_L and T_R for the colder left panel are 400 K and 200 K respectively. Whereas, these initial values for the right panels are 4500 K and 3500 K respectively. The initial fractions of different hydrogen species, (i.e, X_{HI}, X_{H2} and X_{HII}) are set to their equilibrium values corresponding to the temperatures on both sides of the interface (see Fig 2). In both panels, solution obtained using an Ideal EoS is shown as *solid lines*, whereas that obtained using PVTE Law is marked as *stars*. The difference in the position of the shock for the two EoS considered here is very much evident in the left panel. Further, the cooling behind the shock for an ideal EoS is more efficient as compared to that for PVTE Law as seen from two temperature curves. On the other hand, there is negligible difference between the quantities obtained for both EoS on the right panel. Also, the cooling behind the shock is stronger as the temperatures decreases from about 427 K to ∼

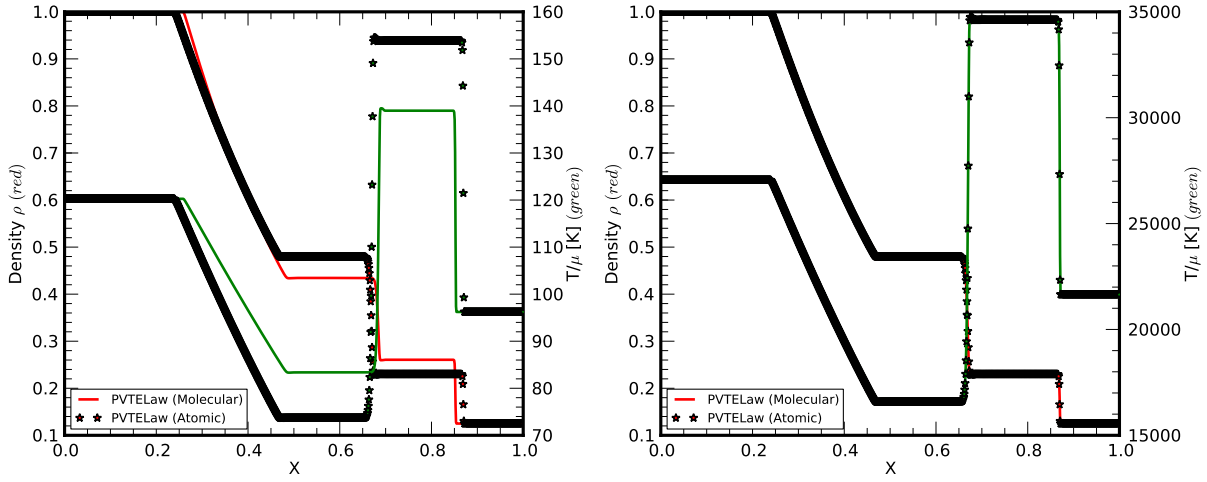

Fig. 5. This figure compares the PVTE Law from DAngelo (*solid line*) and that for Ionized Hydrogen (*star marker*) for two different temperature values. The *left* is the profile for density (red) and ratio of temperature to mean molecular weight (μ) (green) for low temperature value. The same profiles for high temperatures are shown in the *right* panel.

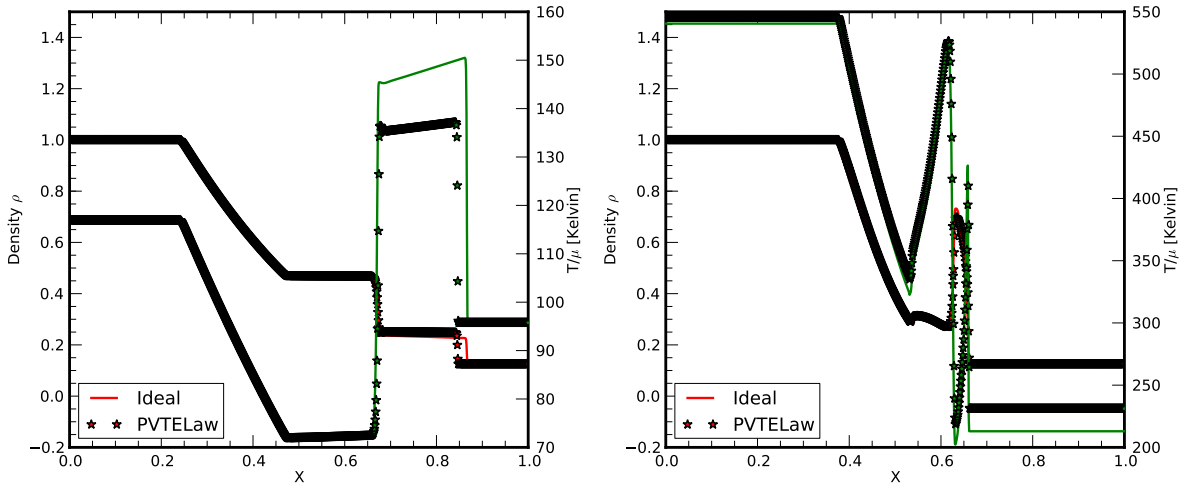

Fig. 6. The figure shows variation of density (*red*) and temperature (*green*) at the final stage of Sod shock tube test for cases which have included explicit cooling. The *solid lines* represent values obtained from Ideal EoS, while those obtained using PVTE Law are marked as *stars*. The left and right panel differ in the value of their initial temperature on either sides of the interface at x = 0.5.

200 K. This is also evident from the compressed density structure.

Such a difference can be attributed to different dependence of internal energy on the gas temperature for cases in thermal equilibrium and that where explicit non-equilibrium cooling is involved. As discussed in Sec. 2.5), with explicit cooling, contribution from terms that are related to degrees of freedom are the ones included to internal energy, U. While, terms corresponding to molecular dissociation or ionization are treated as a components to explicit cooling function, Λ, which are assumed to be radiated away are are common to both EoS. In case, when the initial temperatures on either side of the interface are low (left panel, fig 6), the terms in the internal energy that correspond to molecular degrees of freedom play a vital role. As a result, in case of PVTE Law, part of the energy produced by due to shocks goes in populating these degrees of freedom, while the rest is used to raise the gas temperature. While in case of Ideal EoS, all the energy produced due to shocks can in principle be used to increase the temperature. Since, in this way more energy is available to raise the gas temperature for an Ideal EoS as seen from the temperature at the shock surface of 150 K as compared to 140 K for PVTE Law. Such a colder gas obtained with PVTE Law also shows more compression as compared to its Ideal counterpart as seen from the density variation. Additionally, since the cooling is more effective for larger temperatures, the temperature behind the shock decreases more rapidly for ideal EoS, while its fall is relatively more gradual for PVTE Law.

In case when the initial temperatures are between 3500-4500 K , i.e., where molecular hydrogen dissociates, the thermodynamics is governed by components related to molecular dissociation in the cooling function. Since they are the same of both EoS, very slight difference is observed in the evolution of shock structure at such high temperatures. Physically, this suggests that for gas behind a strong shock discontinuity, translational degrees of freedom are the first to adopt to change. The internal rotational

and vibrational degrees of freedom of H_2 molecule do not seem to play any role. Thereby for gas just behind a sharp discontinuity, it is appropriate to adopt an adiabatic index $\gamma = 5/3$. This is consistent with studies of dissociation due to J-type shocks (e.g., Flower et al. (2003)).

In summary, various cases treated for the study of a standard shock tube test elucidates the critical importance of treating temperature dependent EoS both in case when the system is in equilibrium and also when explicit radiative cooling is involved. In the next sections, we will extend the application of general EoS to some 2D test problems providing further physical insights.

4.2. Gravitational Collapse

The effect of PVTE Law EoS on one-dimensional gravitational collapse of a molecular core is studied under LTE with this test. The initial *sub-critical* core suspended in a hot and less dense environment does not undergo a complete collapse but rather oscillate avoiding extremely large densities at the center, which are difficult to resolve without adaptive mesh refinement. The numerical domain extending up to a radial distance of $r_0 = 0.1$ pc is initialized with a constant density, $\rho_0 = 1.66\times10^{-19}$ g cm^{-3}. The pressure in the domain is set such that the temperature of the initial molecular core is initialized to ~ 40 K. In case of an ideal EoS, a constant value of adiabatic index, $\Gamma = 1.4$ is chosen in consistency with fully molecular gas, whereas, for the PVTE Law EoS, Γ_1 is estimated using Eq.22. Axisymmetric boundary conditions are set at $r = 0$. The ambient medium ($r > r_0$) is in pressure equilibrium with the molecular core, but is hotter due to density contrast, $\rho_{\rm amb}/\rho_0 = 0.65$. The ambient material is injected from the outer boundary with a radial inflow velocity of the form $v_r = v|_{r_0}\sqrt{\left(\frac{r_0}{r}\right)}$. The self gravitational potential is calculated self-consistently as described in Mignone (2014).

At the onset of collapse, the core behaves in a very similar manner for both EoS. The unstable constant density core undergoes a gradual collapse from outside resulting in a steady increase of density in the inner parts. In addition to the density, the pressure (and therefore the temperature) also increases gradually towards the center of the core. The dynamical evolution of the core begins to differ around 0.6 free fall time where the PVTE Law deviates from the Ideal behavior. The collapse continues till about a free fall time beyond which the core rebounds back. Fig. 7 shows the comparison in density and temperature structure of the core at 1.2 free fall time. From the left panel it is evident that the central core obtained with PVTE Law EoS is 5 times denser than that obtained from Ideal EoS. In addition, the core resulting from an Ideal EoS is slightly more extended in radial direction. This is further clarified from the position of shock seen in the temperature plot (right panel; solid lines). The temperature in the center of the core reaches around 300 K for both cases. However, the outer region with ideal EoS, ($T \sim 3000$ K) is two times hotter than that obtained from PVTE Law EoS. This is essentially because, in case of PVTE Law EoS, the gravitational energy released on account of the collapse goes into disassociation of molecules rather than increase of thermal pressure. This is reflected in the value of adiabatic index (right panel; dashed lines) which reaches close to an isothermal limit of unity in this outer region. Lack of thermal pressure support, facilitates further collapse and results in a more dense and compact core as compared to that obtained from Ideal EoS.

4.3. Blast Wave

The newly implemented PVTE Law EoS in case of thermal equilibrium is tested for a 2D Spherical blast wave. The problem is solved on cartesian grid in a square domain of size, $-0.5 < x, y < 0.5$ which is resolved with 300×300 grid points. The blast is initiated at the center of the domain ($x = y = 0.0$), by providing an initial contrast in density and pressure, η and χ respectively, between the blast region ($r_0 < 0.1$) and the surrounding ambient medium. For the present case, we choose $\eta = 10.0$ and $\chi = 20.0$. At the onset of the blast, a shock wave which maintains its spherical shape emerges from the central blast region. Fig. 8 shows the logarithmic values of density at time $\tau = 0.15$. The panel on the left correspond to solution obtained using Ideal EoS, while that obtained using PVTE Law at thermal equilibrium is shown in the middle panel. The density structure in the right panel is also obtained using PVTE Law but with a high order interpolation, (i.e., Piecewise Parabolic) method (PPM) instead of the Piecewise Linear method (PLM) used to produce density structure in the middle panel.

On comparing the left and the middle panel, one can clearly identify the differences between the two EoS considered here. As expected from the study of shock sod tube test, the size of spherical blast wave is smaller in case of solution obtained from PVTE Law. This is due to the lower shock propagation speed as compared to that with an Ideal EoS. Further, the effect of PVTE Law in compression of fluid just behind the shock is very clearly seen in the middle panel. Such a compression is totally absent in the solution obtained using an Ideal EoS. The incorporation of temperature dependent terms in the estimate of internal energy and using it to consistently derive the temperature is therefore verified to mimic *equilibrium cooling*.

Another striking difference between the left and middle panel of Fig. 8, is the formation of prominent ripples in case of Ideal EoS between the intermediate compressed region and outer rarefied medium at four distinct places. This is a typical feature due to noise from the Cartesian grid. However, these ripples are not as prominent in the middle panel. This indicates the applied solver becomes slightly more diffusive with PVTE Law and can not capture typical features due to Cartesian grid, as effectively. However, with a higher order interpolation schemes like the PPM, the PVTE Law begins to show features more clearly (see right panel of Fig. 8).

4.4. Axisymmetric MHD Jets

The effect of PVTE Law on dynamics has also been studied for propagation of axisymmetric magnetized jets in 2D. A cylindrical domain of size (r, z) = (10.0, 60.0) with a resolution of 96×576 grid points has been used for this test problem. Initially, the domain is filled with a static unmagnetized ambient medium with a density of $\rho_a = 10^4$cm^{-3} and a temperature of 2500 K. A magnetized jet is injected into this static medium from the base ($z = 0$) through a nozzle of radius, $R_{\rm jet} \sim 167$ AU. Dense jet material which has a density contrast of 5 with respect to the ambient medium is injected with a velocity of 100 km s^{-1}. The magnetic field in the jet is purely a toroidal one with a field strength $\sim 10\,\mu$G at the axis. The total pressure in the jet is the sum of the thermal (kept same as the ambient medium) and magnetic pressure. The material in the jet is colder than the ambient medium with a temperature of 1000 K.

As the colder jet enters into the hot ambient medium, it immediately results into a formation of bow-shock that pushes the ambient material to it sides. This processed material acquires

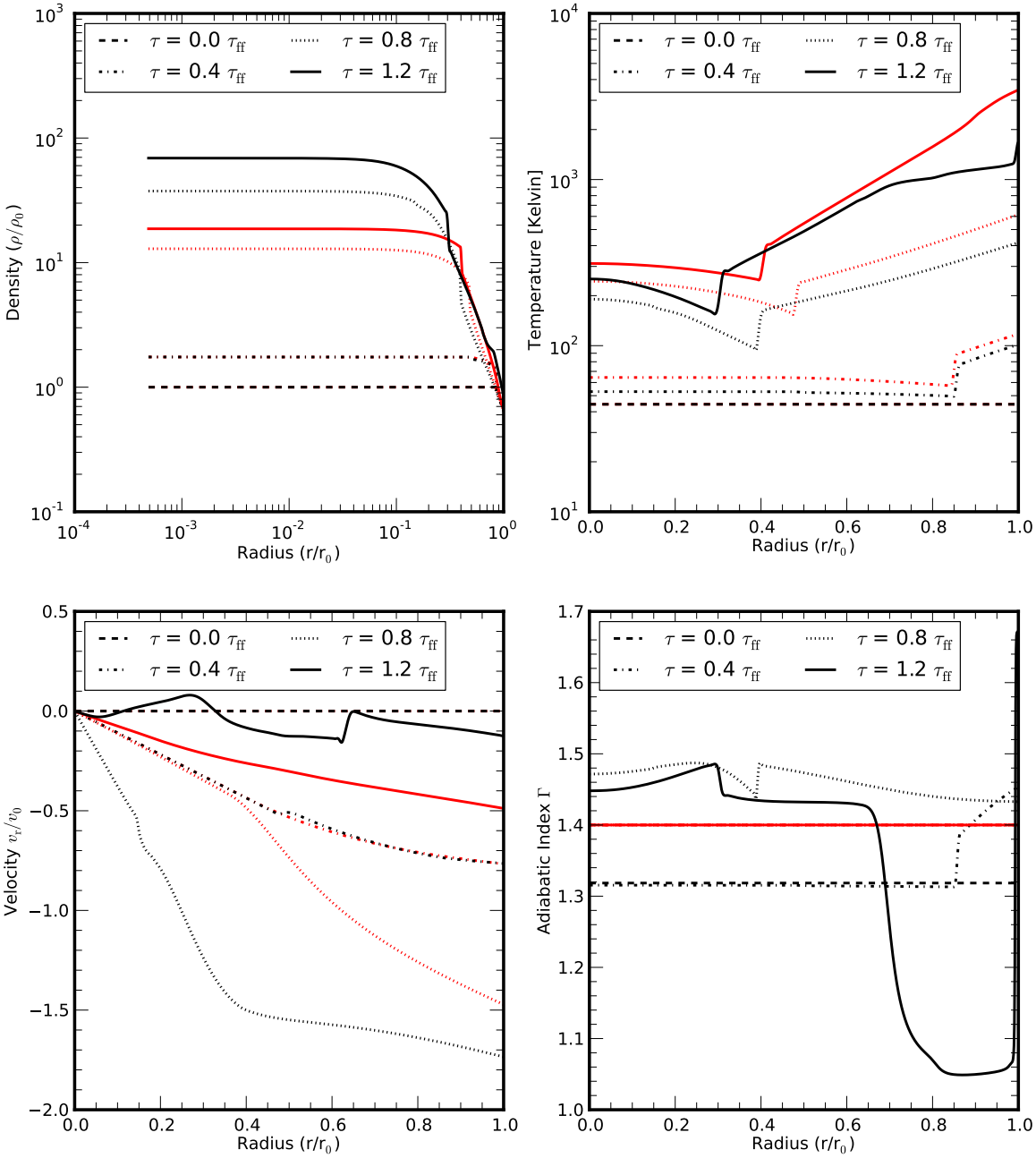

Fig. 7. Dynamical evolution of one-dimensional gravitational collapse with two different EoS. In each of the four panels, *red* colored lines represent values for Ideal EoS, while the quantities obtained with PVTE Law are shown with *black* colored lines. *Top Left* panel shows the logarithmic values of normalized density with radial distance. Temperature in Kelvin and normalized radial velocity are shown in *top right* and *bottom left* panel respectively. The evolution of adiabatic index for PVTE law is shown in the *bottom right* panel, while its value for Ideal remains fixed at all times to $\Gamma = 1.4$. These curves exhibit values of respective quantities at 4 different times, τ relative to the free fall time τ_{ff}, as shown in the legend.

high temperatures and forms the cocoon as shown in the left panel of Fig. 9. The two panels of the figure show the jet structure at time, $\tau = 4.0$ using an Ideal EoS (*left*) and that obtained from PVTE Law (*right*). Each panel is further divided into two halves. The left half show the logarithmic values of temperature in Kelvin, while the right panel shows the corresponding value of density in code units. For both the EoS considered here, the maximum temperature is obtained at the bow-shock. Its value for

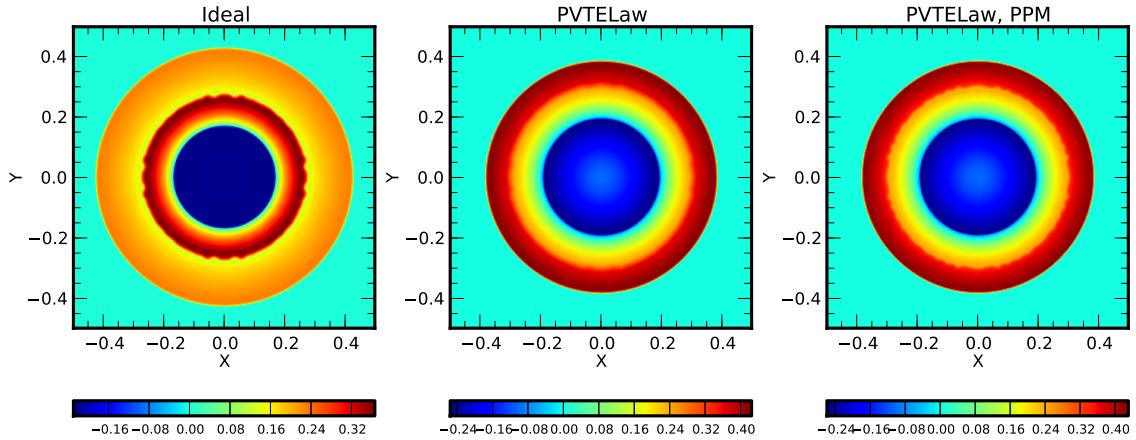

Fig. 8. Comparison of logarithmic values of density ρ (in code units) for a hydrodynamic, spherical blast wave at time $\tau = 0.15$. The *left panel* shows the final shock structure (see text) with an ideal EoS and using linear interpolation and 2nd order Runge-Kutta method for time stepping. The density obtained using the same numerical methods but with a GammaLaw EoS (assuming CIE) is shown in the *middle panel*. The *right panel* is same as the middle one except parabolic interpolation and 3rd order Runge-Kutta time-stepping algorithm are used.

ideal EoS is 1.9e5 K while that for PVTE Law is about a factor of 4 small, 4.8e4 K. On the contrary, the maximum density for the jet obtained with PVTE Law is $1.7 \times 10^6 \mathrm{cm}^{-3}$, higher than its Ideal counterpart by a factor of 10.

In addition to the above quantitative differences for the two EoS considered, the jet structures also differ as evident from the Fig. 9. Firstly, the jet head in the left panel has travelled a larger distance in the same time interval as compared to the jet in right panel. Also, the jet ejected using an Ideal EoS, shows a more broader structure at the base while it tapers close to the bow shock. Whereas, a much narrow jet is obtained on using a PVTE Law EoS. Further, the processed hot cocoon material has larger width (in *density*) in case of jet with an Ideal EoS as compared to that obtained from PVTE Law. This is because the total energy in the cocoon gets distributed into other forms of internal energy (see equation 20) in case of PVTE Law, which *effectively cools* the cocoon material resulting into its collapse into a thin layer on the sides of the jet. This same *equilibrium cooling* effect is also seen at the bow-shock for the jet obtained with PVTE Law. Here, the bow-shock is much more turbulent and forms dense condensates as compared to that obtained for a jet with an Ideal EoS.

4.5. Pulsed Molecular Jets

The application of non-equilibrium cooling due to molecular hydrogen with PVTE Law is studied using hydrodynamic propagation of supersonic pulsations (that eventually form shocks) into molecular medium. This is seen as a common phenomenon in molecular jets ejected from young stellar source. In this test our focus is mainly to study differences in shock structure due to different EoS, therefore, we choose a narrow radial extent (< jet radius) to avoid formation of back-flow and associated instabilities usually seen with such jets. A complete study of instabilities due to cooling and EoS in molecular jets will be taken up in the forthcoming paper.

The test is done using the Adaptive Mesh refinement module developed for PLUTO code (Mignone et al. 2012). The two-dimensional domain in cartesian co-ordinates extends radially from -0.5 r_{jet} to 0.5 r_{jet} and has a vertical extent up to 32 r_{jet}. The domain has a base grid of 4×128 points and with the highest refinement level of 5 resulting in an equivalent grid of 128×4096 zones. Fully molecular ($X_{H2} \approx 0.5$) ambient medium representing a young star-forming core fills the initial domain with a constant temperature of 50 K. The ambient number density decreases with vertical extent, $\rho_{\rm amb}(z) \propto z^{-2}$, its value at z = 0 set to be 10^4 cm^{-3}. An over-dense jet is injected from the nozzle at z = 0 with a jet radius , $r_{jet} \sim 167$ AU. At the nozzle, the jet has a density three times more than the ambient medium. Additionally, the temperature at the nozzle is set at 1000 K resulting in jet pressure to be 60 times higher than the medium (at z =0). The initial hydrogen fractions at the nozzle are estimated based on equilibrium shown in fig.2. The injection velocity has sinusoidal perturbations of the form, $v_{jet} = v_0\,(1.0 + 0.25*\sin(2.0\pi\, t/T_p))$, with base velocity, v_0 is set to be 80 km s^{-1} and pulsation period, T_p of 30 years.

At the onset of simulation, the primary pulse that enters into the domain from the nozzle forms the strongest shock as the temperature reaches up to 10^5 K where hydrogen can ionize forming HII. The successive pulses see a much less pressure jump forming a relatively weaker shocks with temperatures of few 1000 K. As the cooling times in such jets are small as compared dynamical time, the material behind the shock start to radiatively cool as the pulses propagate in the molecular medium. As a result, the initially formed shocks with a very thin width broadens due to loss of energy. Top panel of fig. 10 shows the difference in density for intermediate shocks after $\tau \sim 158$ yr for two EoS considered here. The panel is divided into two halves and the common color bar indicates that the maximum density reached is about 20 times its initial value. The upper half shows the density of three pulses between $15.0 r_{jet} < z < 24.0 r_{jet}$ for PVTELaw EoS and same for Ideal EoS is shown in the bottom half. For each half, the variation in the shock width is evident with height due

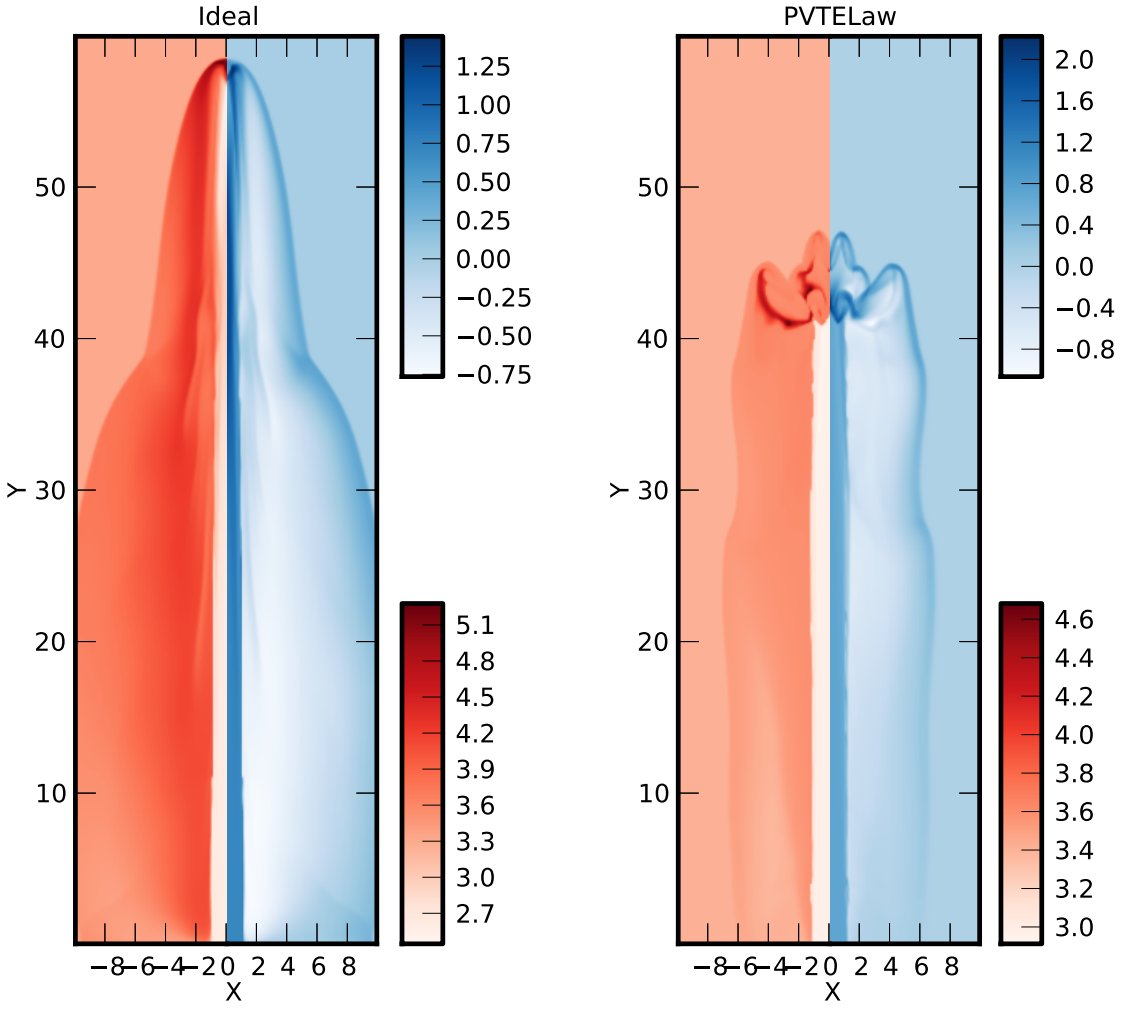

Fig. 9. Comparison of logarithmic values both of density, ρ (right half in *blues*) and temperature in Kelvin (left half in *red*) for a 2D axisymmetric jet without explicit cooling. The *left panel* shows the jet structure with an ideal EoS, while, that obtained from a PVTELaw EoS (assuming CIE) is shown in the *right panel*.

to losses in energy by cooling resulting in temperatures around 100 K behind the shock. In addition, a clear difference in the width is also seen for each shock due to different EoS. Further, one dimensional cuts for pressure and HI fractions at z ∼ 15.8 r_{jet} are shown in the bottom panels.

The bottom panels of fig. 10 clearly shows the width of the shock formed with PVTELaw is smaller as compared to one formed with constant Γ EoS. Additionally, the peak HI fraction density obtained from PVTELaw is about 65% times higher than that obtained from Ideal EoS. The pressure obtained from PVTE is also higher by 35% than its Ideal counterpart. A narrow shock width and enhanced peak value of quantities seen in the shock structure with PVTELaw is consistent with that obtained from the Sod shock tube with cooling with temperatures around 100 K (see left panel of fig. 6). However, the differences are less prominent for primary shock and young shocks (pulsations that have entered the domain), as temperature behind these shocks reach up to 500 K to 1000 K, as seen in the right panel of fig. 6.

5. Summary and Conclusions

We have described an implementation of a thermodynamically consistent EoS in PLUTO code. This chemical EoS, PVTELaw, takes into account various atomic and molecular process both in case of thermodynamic equilibrium and in presence of non-equilibrium cooling. The use of such an EoS with non-constant Γ is essential for a consistent study of astrophysical systems with processes like dissociation, ionization and recombination play a vital role.

The numerical implementation of caloric EoS like the PVTELaw is done with a particular focus on thermally ideal gas, however, it can be also extended to study real gases. Two different strategies, viz. the general root finder and tabulated method, are used to invert caloric EoS to obtain pressure from internal energy at a given temperature and density. We have seen that in certain test problems, the tabulated method achieves a speedup to a factor of 4 with similar accuracy as compared to the root finder method.

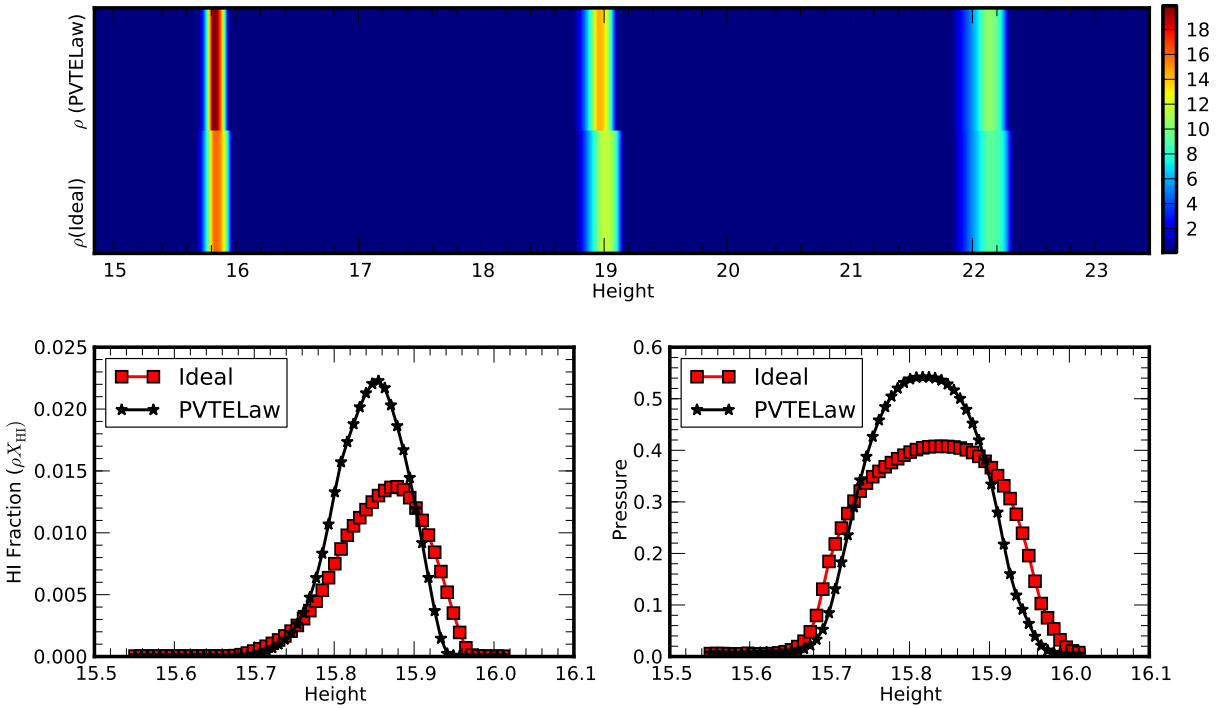

Fig. 10. Results from the test studying the propagation of supersonic pulsations in molecular medium. The *top* panel compares the density obtained for three intermediate shocks at time, τ = 158 yrs, from PVTELaw (top half) and Ideal EoS (bottom half). Radial cuts for HI density fraction and pressure for the shock at z = 15.8 are shown in bottom *left* and *right* panels respectively. The *red squares* are used to represent values obtained from Ideal EoS, while values obtained from PVTE Law are shown with *black stars*.

Further, we have highlighted the importance of spline interpolation of tabulated values. As a bi-linear interpolation, although relatively faster, can be thermodynamically inconsistent producing composite waves.

The standard test of Sod shock tube clearly brings out the difference between distribution of heat into internal energy for the two EoS considered here. In case of mono-atomic Ideal EoS (constant Γ) under the limit of local thermodynamic equilibrium, the energy generated by impact of shock will be only be distributed into 3 translational degrees of freedom while with a general caloric EoS, additional degrees of freedom are available due presence of diatomic molecules. As a result, the heat generated from shock with PVTE Law will not increase the temperature of the gas instead populate rotational and vibrational levels. This effectively results in *equilibrium cooling* of gas leading to compression in density.

A similar physical effect is seen even in presence of non-equilibrium cooling due to molecular hydrogen. In such a case, terms related to degrees of freedom are added to the internal energy while the terms responsible for radiative cooling are added as source term in form of a cooling function, Λ. The differences in width of the shock and value of physical quantities due to EoS, is enhanced for temperatures in range of 100, K. Whereas, for higher temperatures these differences become small as the evolution of internal energy is mainly governed by source terms in the cooling function which are same for both EoS.

In summary, this general implementation of chemical and thermodynamically consistent EoS will prove to be a useful tool to study various astrophysical systems like planet formation, molecular jets from young stars, gravitational collapse of molecular cloud, galaxy formation due to cold flows etc.

References

Abel, T., Anninos, P., Zhang, Y., & Norman, M. L. 1997, New A, 2, 181
Black, D. C., & Bodenheimer, P. 1975, ApJ, 199, 619
Boley, A. C., Hartquist, T. W., Durisen, R. H., & Michael, S. 2007, ApJ, 656, L89
Cen, R. 1992, ApJS, 78, 341
Clayton, D. D. 1984, Principles of stellar evolution and nucleosynthesis. (The University of Chicago Press)
D'Angelo, G., & Bodenheimer, P. 2013, ApJ, 778, 77
Flower, D. R., Le Bourlot, J., Pineau des Forêts, G., & Cabrit, S. 2003, MNRAS, 341, 70
Galli, D., & Palla, F. 1998, A&A, 335, 403
Glover, S. C. O., & Abel, T. 2008, MNRAS, 388, 1627
Hollenbach, D., & McKee, C. F. 1979, ApJS, 41, 555
Jappsen, A.-K., Klessen, R. S., Larson, R. B., Li, Y., & Mac Low, M.-M. 2005, A&A, 435, 611
Li, Y., Klessen, R. S., & Mac Low, M.-M. 2003, ApJ, 592, 975
Menikoff, R., & Plohr, B. J. 1989, Reviews of Modern Physics, 61, 75
Mignone, A. 2014, Journal of Computational Physics, 270, 784
Mignone, A., Bodo, G., Massaglia, S., et al. 2007, ApJS, 170, 228
Mignone, A., Zanni, C., Tzeferacos, P., et al. 2012, ApJS, 198, 7
Nannan, N., Guardone, A., & Colonna, P. 2013, Fluid Phase Equilibria, 337, 259
Omukai, K., & Nishi, R. 1998, ApJ, 508, 141
Palla, F., Salpeter, E. E., & Stahler, S. W. 1983, ApJ, 271, 632
Press, W. H., Teukolsky, S. A., Vetterling, W. T., & Flannery, B. P. 2007, Numerical Recipes 3rd Edition: The Art of Scientific Computing, 3rd edn. (New York, NY, USA: Cambridge University Press)
Smith, M. D., & Rosen, A. 2003, MNRAS, 339, 133
Spaans, M., & Silk, J. 2000, ApJ, 538, 115
Teşileanu, O., Mignone, A., & Massaglia, S. 2008, A&A, 488, 429
Wolberg, G., & Alfy, I. 2002, Journal of Computational and Applied Mathematics, 143, 145
Woodall, J., Agúndez, M., Markwick-Kemper, A. J., & Millar, T. J. 2007, A&A, 466, 1197
Yoshida, N., Omukai, K., Hernquist, L., & Abel, T. 2006, ApJ, 652, 6

Appendix A: Cubic Interpolation

When a cubic spline is used, Eq. (34) is inverted in the following way. First gather the coefficient of the two cubic in the interval $[y_j, y_j + 1]$:

$$\tilde{a}x^3 + \tilde{b}x^2 + \tilde{c}x + \tilde{d} = 0 \tag{A.1}$$

where

$$\begin{aligned} \tilde{a} &= a_{i,j}(1 - y_j) + a_{i,j+1}y_j \\ \tilde{b} &= b_{i,j}(1 - y_j) + b_{i,j+1}y_j \\ \tilde{c} &= c_{i,j}(1 - y_j) + c_{i,j+1}y_j \\ \tilde{d} &= d_{i,j}(1 - y_j) + d_{i,j+1}y_j - \rho e \end{aligned} \tag{A.2}$$

We then simplify the cubic as

$$x^3 + \alpha x^2 + \beta x + \gamma = 0 \tag{A.3}$$

where $\alpha = \tilde{b}/\tilde{a}, \beta = \tilde{c}/\tilde{a}, \gamma = \tilde{d}/\tilde{a}$.

The number of real roots of the cubic depends on the sign of $Q^3 - R^2$, where

$$Q = \frac{\alpha^2 - 3\beta}{9}, \qquad R = \frac{2\alpha^3 - 9\alpha\beta + 27\gamma}{54} \tag{A.4}$$

We distinguish among the following cases:

- when $Q^3/R^2 > 1$ the cubic has three real roots (Press et al. 2007) given respectively by:

$$\begin{aligned} x_1 &= -2\sqrt{Q}\cos\left(\frac{\theta}{3}\right) - \frac{\alpha}{3} \\ x_2 &= \sqrt{Q}\left[\cos\left(\frac{\theta}{3}\right) - \sqrt{3}\sin\left(\frac{\theta}{3}\right)\right] - \frac{\alpha}{3} \\ x_3 &= \sqrt{Q}\left[\cos\left(\frac{\theta}{3}\right) + \sqrt{3}\sin\left(\frac{\theta}{3}\right)\right] - \frac{\alpha}{3} \end{aligned} \tag{A.5}$$

  where

$$\theta = \mathrm{acos}\left(\frac{R}{\sqrt{Q^3}}\right). \tag{A.6}$$

  Since $0 \le \theta \le \pi$ (by definition) it can be verified that the three real roots given by Eq. (A.5) always satisfy $x_1 \le x_2 \le x_3$. In addition, knowing that the spline is monotonically *increasing* between T_i and T_{i+1} (or $x \in [0, 1]$), we can easily select the desired root:
  - when $\tilde{a} > 0$, only x_1 or x_3 can be valid roots since the cubic is monotonically decreasing at x_2. In order to select the correct one, we look at the inflection point $x_f = -\alpha/3$: when $x_f > 1$ we pick x_1 whereas if $x_f < 0$ we pick x_3 (note that x_f can never fall in the interval $[0, 1]$ by construction).
  - when $\tilde{a} < 0$, the cubic is monotonically increasing only between the segment connecting the two extrema and therefore x_2 is the only admissible root.
- when $Q^3/R^2 < 1$, the cubic has only one real root which is readily computed from

$$x_1 = (A + B) - \frac{\alpha}{3} \tag{A.7}$$

  where

$$A = -\mathrm{sign}(R)\left[|R|\left(1 + \sqrt{1 - \frac{Q^3}{R^2}}\right)\right]^{1/3}, \tag{A.8}$$

  and $B = Q/A$.

Appendix B: Fundamental Gas Derivative & Composite Waves

In section 3, two basic strategies used to numerically invert the caloric EoS are described viz., the iterative root-finder method and the lookup table method. Further for the lookup table method, two different interpolation methods (linear and spline) are used to connect the adjacent nodes. Interpolation methods are indeed faster than the iterative root-finder but they need to be formulated carefully to ensure consistency with thermodynamic principles for an ideal poly-tropic gas. A through analysis of each of these interpolation methods is done via an estimation of *fundamental gas derivative*.

The *fundamental gas derivative*, denoted by $\mathcal{G}$, is a non-dimensional form that represents the non-linear variation of the speed of sound with respect to density under constant entropy, s, and can be expressed as

$$\mathcal{G} = 1 + \frac{\rho}{c}\left(\frac{\partial c}{\partial \rho}\right)_s. \tag{B.1}$$

Here, ρ is the density and the speed of sound, c is given by

$$c = \sqrt{\left(\frac{\partial P}{\partial \rho}\right)_s} \tag{B.2}$$

with P being the gas pressure. An ideal poly-tropic gas satisfying the thermodynamical constraints has the positive value of $\mathcal{G} = \frac{\gamma+1}{2} > 0$. This implies that such a gas has a *convex* isoentrope in the P-v plane (v being the specific volume) and will only admit compression shock waves and expansion fans. However in case of real gases, $\mathcal{G}$ can as well have negative values relating to finite interval of *concave* P-v isoentropes. This enables such gases to admit *composite waves* in addition to standard expansion fans and compressive shock waves, whilst satisfying the thermodynamical principles (e.g. Menikoff & Plohr 1989, and references therein). Using standard thermodynamic relations, equation B.1 can be expressed as a function of ρ and temperature, T, (Nannan et al. 2013)

$$\mathcal{G} = \frac{1}{2c^2\rho^3}(\Gamma_1 + \Gamma_2 + \Gamma_3) \tag{B.3}$$

where the thermodynamic speed of sound, c, is computed from

$$c^2 = \left(\frac{\partial P}{\partial \rho}\right)_T + \frac{T}{C_v\rho^2}\left(\frac{\partial P}{\partial T}\right)_\rho^2 \tag{B.4}$$

and the three Γ's are given by,

$$\Gamma_1 = \rho^4\left(\frac{\partial^2 P}{\partial \rho^2}\right)_T + 2\rho^3\left(\frac{\partial P}{\partial \rho}\right)_T \tag{B.5}$$

$$\Gamma_2 = 3\frac{T\rho^2}{C_v}\left(\frac{\partial P}{\partial T}\right)_\rho\left(\frac{\partial^2 P}{\partial \rho \partial T}\right)_{T,\rho} \tag{B.6}$$

$$\Gamma_3 = \left[\frac{T}{C_v}\left(\frac{\partial P}{\partial T}\right)_\rho\right]^2 \times \left[3\left(\frac{\partial^2 P}{\partial T^2}\right)_\rho + \frac{1}{T}\left(\frac{\partial P}{\partial T}\right)_\rho\left(1 - \frac{T}{C_v}\left(\frac{\partial C_v}{\partial T}\right)_\rho\right)\right] \tag{B.7}$$

where, C_v denotes specific heat capacity at constant volume.

In particular, we present here the analysis done for interpolation methods in case of ionized hydrogen gas, where the *internal energy* is given by,

$$e = \frac{3}{2}k_bT + \chi \tag{B.8}$$

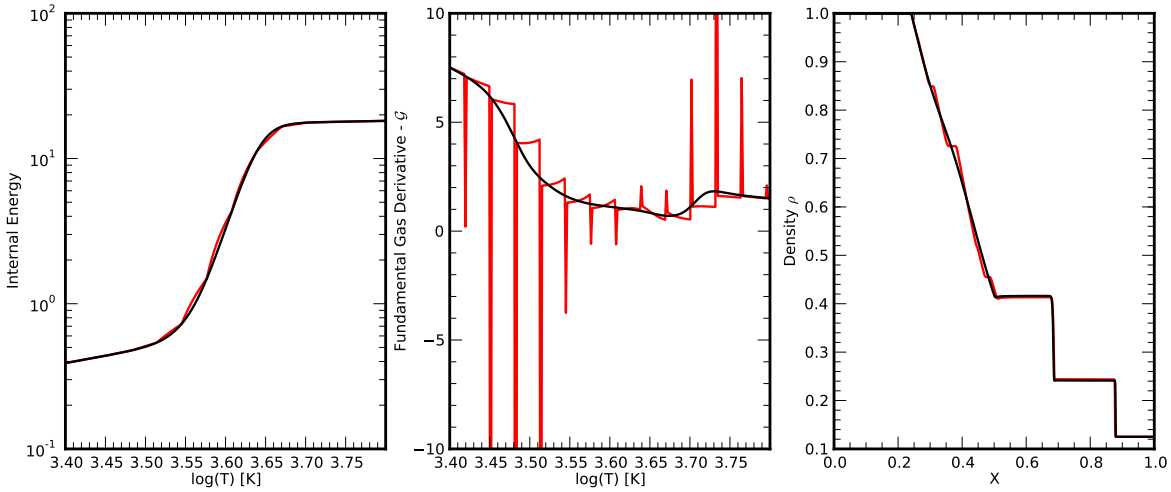

Fig. B.1. Analysis of Linear interpolation method used in the estimate of internal energy. *Left* panel shows the transition region of the internal energy defined by equation B.8. The exact value, *black solid line* is obtained from the iterative root-finder method and the piece-wise linearly interpolated curve is shown as a *red solid line*. The *fundamental gas derivative*, $\mathcal{G}$ is shown in the middle panel. Here, again the *black line* is derived using the estimate of internal energy using the iterative root-finder method, while the *red* curve is that obtained from linear interpolation. *Right* panel compares the exact (*black*) and the interpolated (*red*) standard shock tube solution (only density at time $\tau = 0.2$).

where, χ is the ionization energy for hydrogen. The variation of internal energy for such a gas shows a sharp increase in value around temperatures of 4000 K. The left panel of figure B.1 shows how this sharp transition is sampled if 256 points are used for piecewise linear interpolation in the whole range. Evidently the transition region is poorly sampled and the interpolation curve shows presence of *kinks*. Further with linear interpolation, neither the first derivative or the second derivative of internal energy with temperature is continuous. This is clearly seen as spikes in the *red* curve of $\mathcal{G}$ (middle panel), which depends on the values of these derivatives with temperature in form of C_v. These kinks in the interpolated curve does not preserve the actual convexity leading to negative values of $\mathcal{G}$. In order words, the sound speed across the kink does not remain continuous resulting into *composite waves* as seen in the rarefaction branch of the shock tube test in the right most panel of the figure (*red* curve). The number of kinks are reduced on increasing the number of sample points for linear interpolation to 512, however, the spikes still remain in the estimation of $\mathcal{G}$ due to discontinuous derivatives and so does the composite waves in the solution of shock test tube. While in case of spline interpolation with 512 points, the sampling of internal energy is more accurate and also the derivatives are continuous giving a much smooth profile of $\mathcal{G}$ (see figure B.2), which further translates into a single rarefaction wave without any composite waves which overlaps with the one obtained from iterative root-finder approach.

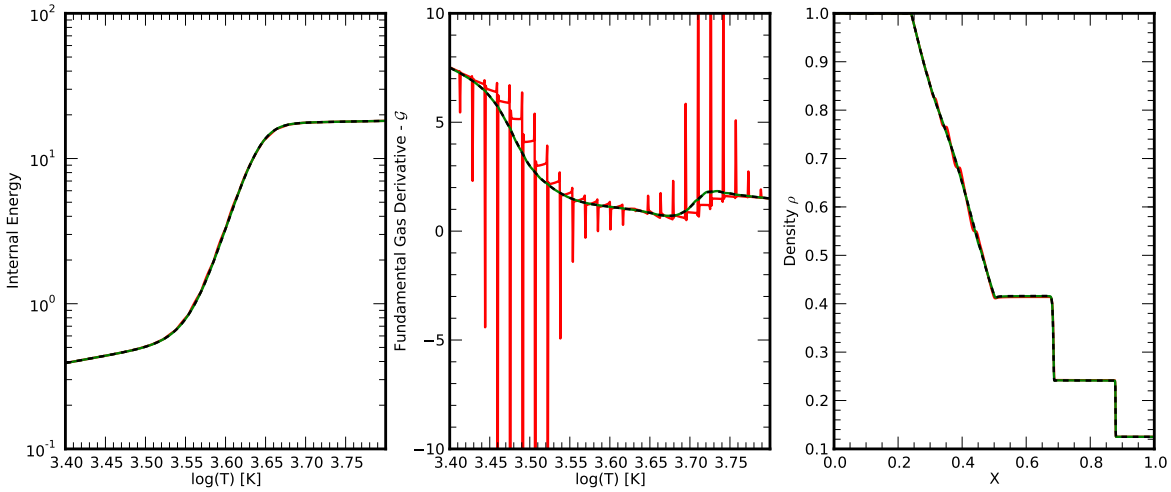

Fig. B.2. Analysis of Spline interpolation method used in the estimate of internal energy and its comparison with piece-wise linear interpolation with 512 sample points. *Left* panel shows the transition region of the internal energy defined by equation B.8. The exact value, *black dashed line* is obtained from the iterative root-finder method, the piece-wise linearly interpolated curve is shown as a *red solid line* and the spline interpolant is shown as a *green solid line*. The *fundamental gas derivative*, $\mathcal{G}$ is shown in the middle panel. Here, again the *black line* is derived using the estimate of internal energy using the iterative root-finder method, while the *red* and *green* curve are obtained from linear interpolation and spline interpolation respectively. *Right* panel compares the exact (*black*), the linearly interpolated (*red*) and the spline interpolated (*green*) standard shock tube solution (only density at time $\tau = 0.2$).